Journal of Nuclear Materials 401 (2010) 78–85

Contents lists available at ScienceDirect

Journal of Nuclear Materials

journal homepage: www.elsevier.com/locate/jnucmat

Effects of beam offset on mechanical properties and corrosion resistance of Alloy 690–SUS 304L EBW joints for nuclear power plant

Yong-Ding Lin [a,1], Hwa-Teng Lee [b,*], Tsung-Yuan Kuo [c,2], Sheng-Long Jeng [d,3], Jia-Lin Wu [b,4]

[a] Department of Mechanical Engineering, Nan Jeon Institute of Technology, Tainan 737, Taiwan, ROC
[b] Department of Mechanical Engineering, National Cheng Kung University, Tainan 701, Taiwan, ROC
[c] Department of Mechanical Engineering, Southern Taiwan University, Tainan 710, Taiwan, ROC
[d] Nuclear Fuel and Materials Division, Institute of Nuclear Energy Research, Longtan 32546, Taiwan, ROC

ARTICLE INFO

Article history:
Received 1 June 2007
Accepted 3 April 2010

ABSTRACT

The current study investigates the effect of the beam offset (BOF) on the microstructure, mechanical properties, and the corrosion resistance of the fusion zone (FZ) of Alloy 690–SUS 304L stainless steel (SS) dissimilar metal butt joints formed by electron beam welding (EBW). The experimental results showed that as the value of the BOF increased from 0 to 0.30 mm, i.e. the electron beam shifted progressively toward the Alloy 690 base metal (BM), the tensile strength of the FZ fell from 582.1 to 541.2 MPa. However, the modified Huey test results indicated that the interdendritic corrosion resistance of the FZ was significantly enhanced. Pit nucleation potential value (E_{np}) was raised from 385 to 1050 mV. An offset of 0.30 mm appears to be the optimal BOF setting when fabricating Alloy 690–SUS 304L SS dissimilar metal butt joints using the EBW technique.

1. Introduction

Nickel-based alloy and austenitic stainless steel (SS) are widely used in the fabrication of components designed for boiling water reactors and pressurized water reactors in nuclear power plants. However, according to a review of the operating records maintained by nuclear power plants [1], components formed by the dissimilar welding of nickel-based Alloy 600 and SUS 308 SS are prone to stress corrosion cracking. One of the primary causes of these cracks is thought to be a chromium depletion effect at grain boundaries as a result of the high number of welding cycles (and consequently, the high total heat input) required to fabricate a joint of sufficient strength. Furthermore, the high heat input during the welding process prompts carbide precipitation in both the fusion zone (FZ) and the heat-affected zone (HAZ), and this further increases the propensity of the grain boundary to undergo chromium depletion.

The chromium content of Alloy 690 (29 wt.%Cr–59 wt.%Ni–10 wt.%Fe–0.02 wt.%C) is almost twice that of Alloy 600 (16 wt.%Cr–75 wt.%Ni–8 wt.%Fe–0.023 wt.%C) [2–4]. Thus, replacing Alloy 600 with Alloy 690 is an effective means of combating the problem of chromium depletion in nickel-based weldments [5]. Furthermore, SUS 304L SS (18 wt.%Cr–8 wt.%Ni–72 wt.%Fe–0.013 wt.%C) has a much lower carbon content than SUS 308 SS (19 wt.%Cr–10 wt.%Ni–70 wt.%Fe–0.08 wt.%C), and therefore carbide precipitation in the FZ of the weldment is significantly reduced under equivalent welding conditions. In the current study into the mechanical properties and corrosion resistance characteristics of dissimilar nickel-based alloy and austenitic stainless steel joints, Alloy 600 was replaced with Alloy 690, and SUS 304L SS was used in place of SUS 308 SS.

The nickel-based alloy and austenitic SS components used in nuclear power plants are generally fabricated using traditional welding processes such as shielded metal arc welding (SMAW) and gas metal arc welding (GMAW). In such welding processes, the number of passes required to form a joint of sufficient strength increases in direct proportion to the component thickness. However, the increased heat input into the weldment as a result of the higher number of welding passes prompts carbide precipitation at the grain boundaries and leads to the formation of chromium depletion zones in the FZ. As a result, the corrosion resistance of the weldment is significantly impaired [6–14].

Electron beam welding (EBW) is a high-energy-density beam welding technique capable of welding thick components in a single pass. EBW has a number of key advantages compared to traditional welding processes, including a lower total heat input, a smaller HAZ, a higher depth-to-width ratio, and a lower residual stress. Furthermore, EBW can produce a deep weld much more easily than

E-mail addresses: yungding@mail.njtc.edu.tw (Y.-D. Lin), htlee@mail.ncku.edu.tw (H.-T. Lee), tykuo@mail.stut.edu.tw (T.-Y. Kuo), sljeng@iner.gov.tw (S.-L. Jeng), formula_wu@yahoo.com.tw (J.-L. Wu).
[1] Tel.: +886 6 6523111x3342; fax: +886 6 6533847.
[2] Tel.: +886 6 2533131x3511; fax: +886 6 2537912.
[3] Tel.: +886 3 4711400x6608; fax: +886 3 4711409.
[4] Tel.: +886 6 2757575x62122; fax: +886 6 2745698.

0022-3115/$ - see front matter © 2010 Elsevier B.V. All rights reserved.
doi:10.1016/j.jnucmat.2010.04.001

LBW. Importantly, the overall effect of these individual advantages is to reduce the welding stress and to suppress stress corrosion cracking in the FZ. Therefore, EBW not only has a high welding efficiency, resulting in a shorter welding time, but also provides the means to enhance the reliability and safety of the welded components used in nuclear power plants [15–18].

The corrosion resistance of nickel-based Alloy 690 is known to be significantly better than that of SUS 304L SS [8,11–13]. Furthermore, shifting the centerline of the electron beam toward the Alloy 690 BM during the EBW fabrication of Alloy 690–SUS 304L SS dissimilar joints yields a considerable improvement in the corrosion resistance of the weldment since it increases the amount of Ni and Cr in the FZ. However, the effects of such centerline shifting of the electron beam on the mechanical properties of the joint are not well documented in the literature. Therefore, the objective of the current study is to investigate the effect of the beam offset (BOF) on the microstructure and elemental composition of the FZ in Alloy 690–SUS 304L SS dissimilar metal butt joints fabricated by EBW. The results were then correlated with the mechanical properties and corrosion resistance characteristics of dissimilar weldments fabricated using different BOF parameter settings.

2. Materials and experimental procedure

The Alloy 690 used in the present study was supplied by Sumitomo Metal Technology, Japan, in plate form. Prior to delivery, the alloy had been solution heat treated at 1050 °C for 5 min and then quenched in water. The SUS 304L SS was heat treated in a vacuum at 1050 °C for 80 min and then allowed to cool in nitrogen gas prior to delivery. The compositional details of the two alloys are summarized in Table 1. The BM materials were machined into plates measuring $70 \times 70 \times 3$ mm and dissimilar weldments were then fabricated without any filler metal using an EBW process with the parameters specified in Table 2. Fig. 1 presents a schematic illustration of the design of the weldment.

Samples for microstructural analysis were polished mechanically and were etched electrolytically using a 6 V direct current for 12–20 s in a reagent of 70 ml H_3PO_4 + 30 ml H_2O. Microstructural observations and compositional analysis were performed using a field-emission scanning electron microscope (Philips XL-40FEG SEM) equipped with an Energy Dispersive X-ray Spectrometer (EDS) and an Electron Probe X-ray Micro Analyzer (JEOL JXA-8900R EPMA) integrated with a Wavelength Dispersive X-ray Spectrometer (WDS). Foils for transmission electron microscopy (TEM) analysis were thinned by dipping them in an electrolytic solution comprising 10% $HClO_4$ and 90% alcohol (C_2H_5OH) at a tem-

Table 2
Welding parameters used in EBW process.

Vacuum torr	Voltage (kV)	Current (mA)	Power (W)	Welding speed (mm s^{-1})	Heat input (kJ mm^{-1})
6×10^{-5}	50	26	1300	35	3.71×10^{-2}

Heat input = (voltage × current)/welding speed.

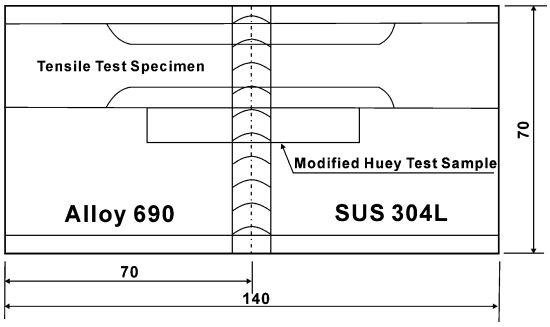

Fig. 1. Design of weldment (units: mm).

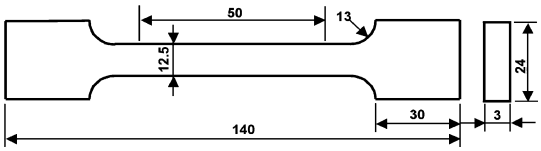

Fig. 2. Tensile test specimen design (units: mm).

Table 3
Thermophysical properties of Alloy 690 and SUS 304L SS.

Temperature (°C)	Inconel 690		SUS 304L SS	
	Specific heat (J/kg °C)	Thermal conductivity (W/m °C)	Specific heat (J/kg °C)	Thermal conductivity (W/m °C)
600	604	22.9	581	22.2
700	631	24.8	594	23.8
800	658	26.6	609	25.4
900	684	28.5	621	27.0
1000	711	30.1	634	28.6

Melting point – Alloy 690: 1343–1377 °C; SUS 304L SS:1398–1454 °C.

Table 1
Elemental compositions of Alloy 690 and SUS 304L SS base metals (wt.%).

Base Metal	Cr	Ni	Fe	C	Si	Mn	P	S	Ti	Cu	Al	Co	Mo	V
Alloy 690	28.73	Bal.	10.01	0.02	0.26	0.31	0.01	0.001	0.30	0.02	0.12	0.014	–	–
SUS 304L	17.88	8.22	Bal.	0.013	0.61	1.62	0.024	0.003	–	0.08	–	–	0.06	0.09

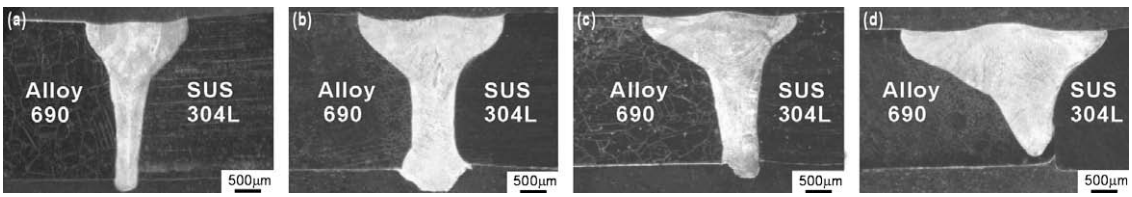

Fig. 3. Optical micrographs of weldments formed using different beam offsets (BOFs): (a) BOF = 0 mm, (b) BOF = 0.15 mm, (c) BOF = 0.30 mm and (d) BOF = 0.50 mm.

perature of −10 °C. Microstructural analyses of the precipitates in the FZ were performed using carbon extraction replicas made by an extraction replication technique [19]. Meanwhile, microstructural analyses of the weldment were performed using TEM, Selected Area Diffraction Patterns (SADPs) and EDS (Philips Tecnai F20 STEM) using a voltage of 200 kV.

The mechanical properties of the various weldments were evaluated by performing tensile tests at a strain rate of 4×10^{-4} s^{-1} under room temperature conditions using an MTS 810 universal tensile test machine. Fig. 2 presents a schematic illustration of the tensile test specimen configuration. As shown, the specimen dimensions were in accordance with the ASTM-E8 specification. Following fracture, the fracture surfaces were observed with SEM.

The corrosion resistance characteristics of the weldments were evaluated with modified Huey and potentiodynamic polarization tests. Initially, the interdendritic corrosion resistance of each weldment was assessed using a modified Huey test, in which samples extracted from the weldments were mechanically polished and then etched in a solution of 65% nitric acid (HNO_3) + 0.1% hydrofluoric acid (HF) at 117 °C for 4 h. The sample surfaces were then examined by SEM to investigate the extent of interdendritic corrosion.

The susceptibility of the weldments to corrosion pitting was evaluated by conducting potentiodynamic polarization tests in a 0.01 M $Na_2S_2O_3$ + 1wt NaCl solution. Specimens were cut from the FZ of each weldment and were mechanically ground and then polished using 1000-grit SiC paper. The specimens were then cleaned ultrasonically in an acetone solution, rinsed in water and then allowed to dry in air. The potentiodynamic polarization tests were performed using an EG&G PARC Potentiostat/Galvanosstat

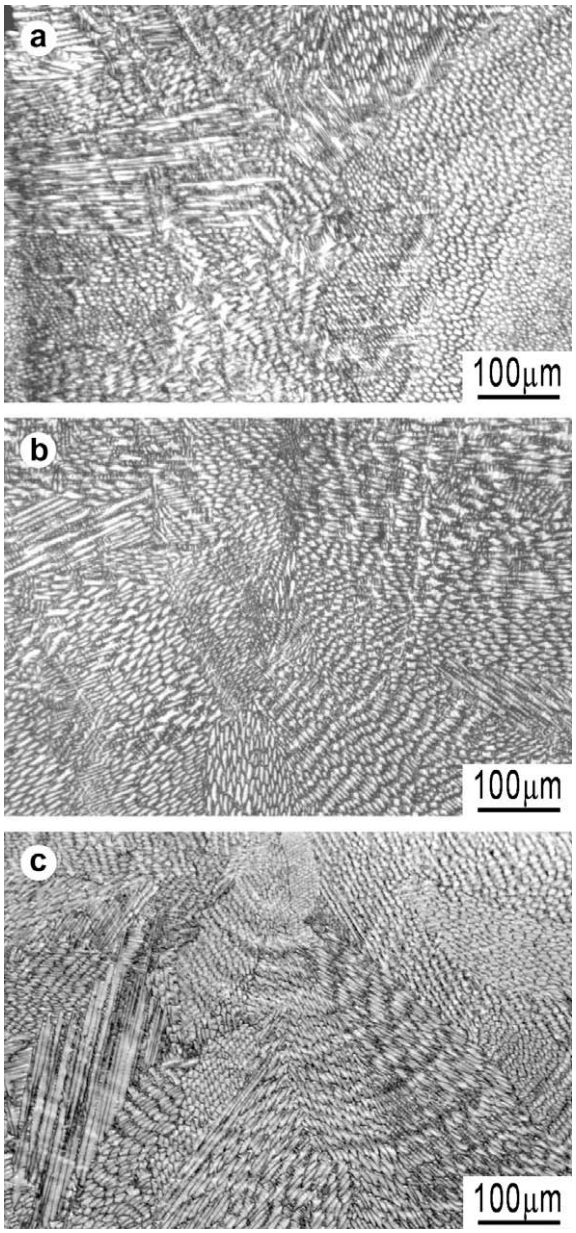

Fig. 4. Micrographs of central region of FZ in weldments formed using different BOFs: (a) BOF = 0.00 mm, (b) BOF = 0.15 mm and (c) BOF = 0.30 mm.

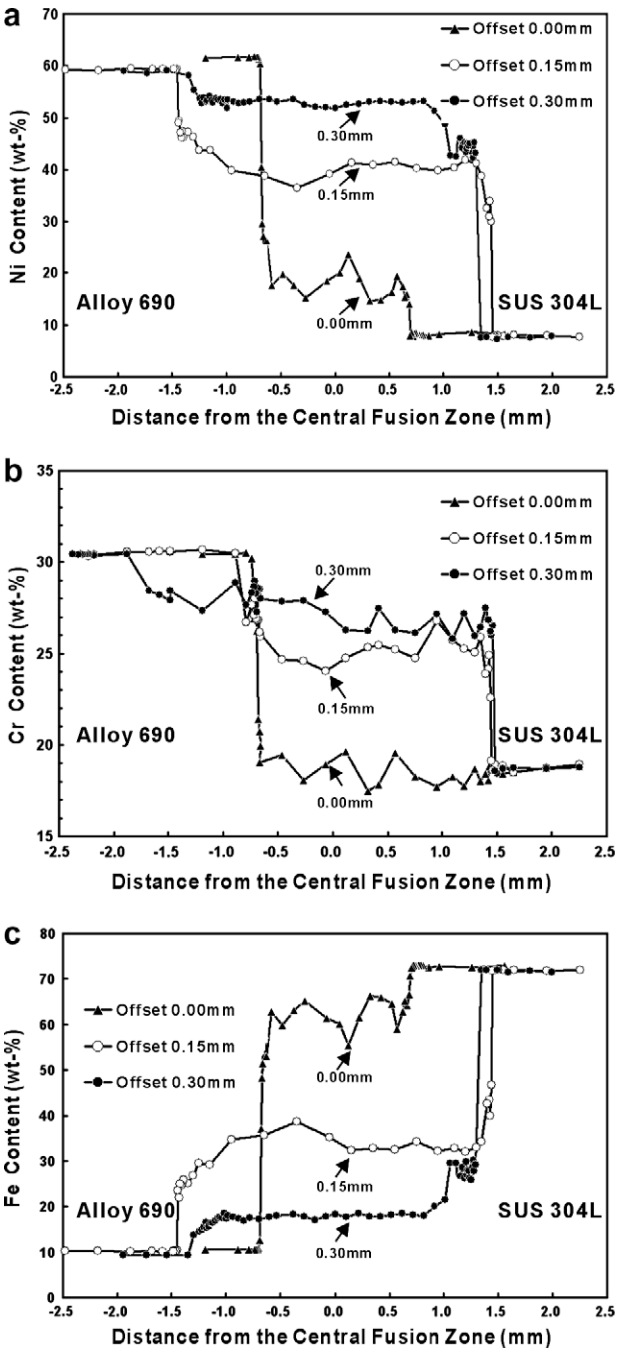

Fig. 5. Compositional analysis results obtained in EPMA line scans from Alloy 690 BM across FZ to SUS 304L SS BM in cap of weldments formed using BOFs of 0, 0.15 and 0.30 mm, respectively: (a) Ni, (b) Cr and (c) Fe contents.

(Model 273). Prior to each polarization test, the 0.01 M $Na_2S_2O_3$ + 1wt.% NaCl solution was deaerated with nitrogen. The tests were conducted using a saturated calomel electrode (SCE) at ambient temperature as the reference electrode, and a platinum mesh as the counter electrode.

3. Results and discussion

3.1. Microstructure of FZ

Fig. 3 presents a series of optical micrographs of Alloy 690–SUS 304L SS weldments fabricated using BOFs of 0, 0.15, 0.30 and 0.50 mm, respectively. Note that a higher BOF value indicates a greater shift of the electron beam toward the Alloy 690 BM. It was observed that the cap region of the weldment on the Alloy 690 side of the weldment expanded as the value of the BOF increased. This expansion effect reflects the greater heat input into the Alloy 690 side and less heat input into the SUS 304L SS side of the weldment at higher BOF values.

As shown in Table 3, the thermal conductivity and specific heat of Alloy 690 were slightly higher than those of SUS 304L SS, and hence when the electron beam was located centrally between the two BMs, i.e. BOF = 0, the SUS 304L SS BM melted to a greater extent than the Alloy 690 BM. As a result, the FZ was offset slightly toward the SUS 304L SS side of the weldment (Fig. 3(a)). However, as the electron beam was progressively shifted toward the Alloy 690 BM, i.e. the BOF parameter is increased from 0 to 0.50 mm, the increased heat input on the Alloy 690 BM side resulted in a greater expansion of the FZ toward the Alloy 690 BM side than toward the SUS 304L SS side (Fig. 3(b–d)). Salminen et al. [20] re-

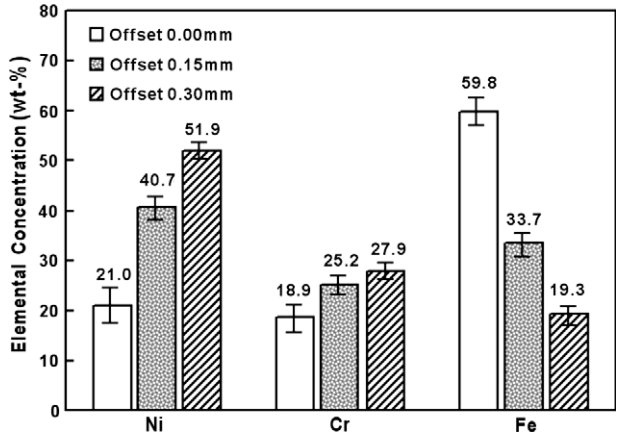

Fig. 6. Average concentrations of Ni, Cr and Fe in FZ of weldments formed using BOFs of 0, 0.15 and 0.30 mm, respectively. (Note that the data represent the average of a series of measurements taken at intervals of 0.05 mm across the FZ.)

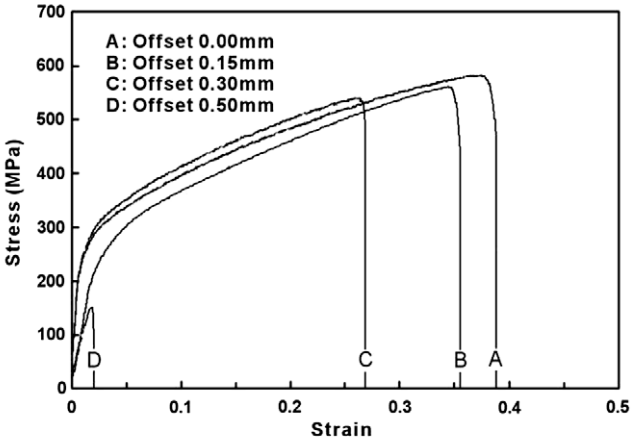

Offset	T.S. (MPa)	Elongation (%)	Fracture Position
Offset=0.00mm	582.1	38.8	Fusion Zone
Offset=0.15mm	559.7	35.8	Fusion Zone
Offset=0.30mm	541.2	27.1	Fusion Zone
Offset=0.50mm	152.5	2.12	Fusion Zone*

*The fusion zone is lack of fusion.

Fig. 7. Stress–strain curves of weldments formed using BOFs of 0, 0.15, 0.30 and 0.50 mm, respectively.

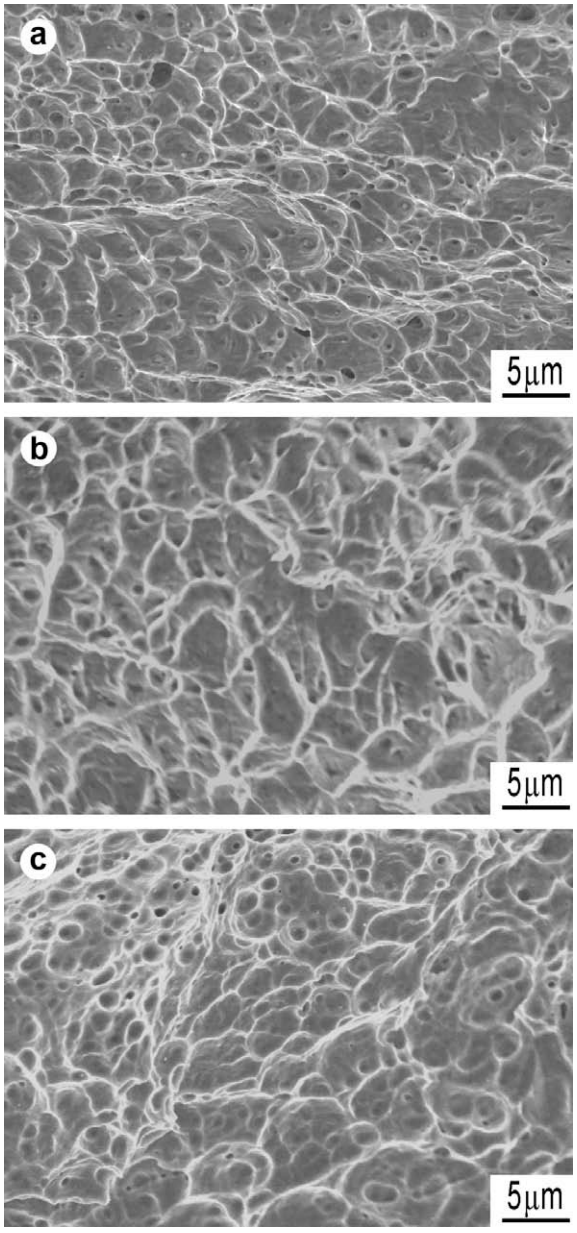

Fig. 8. Scanning electron fractographs of cap weld face of ruptured tensile specimens formed using BOFs of (a) 0.00 mm, (b) 0.15 mm and (c) 0.30 mm.

ported that during electron or laser beam butt welding, the gap has a similar effect as the keyhole in the electron or laser beam welding techniques. The gap suppresses welding heat losses via conduction, thereby enhancing the absorptivity of energy into the workpiece. Consequently, the electron beam penetrates deeply into the weldment, creating a strong melting effect. However, when the electron beam is offset significantly toward the Alloy 690 BM side of the weldment, the electron beam cannot penetrate very far into the weldment because the gap offers no assistance (see Fig. 3(d)). Fig. 4 presents micrographs of the central region of the FZ in weldments formed using BOFs of 0, 0.15 and 0.30 mm, respectively. Since the welding speed and the total heat input remain constant in the current EBW process, the cooling rate in the FZ was identical in each specimen, and thus the BOF had no significant effect on the size of the dendrites or on the arm spacing of the dendrites in this region of the FZ. From an inspection of the three micrographs, it is revealed that the FZs of the three specimens comprised primarily columnar and cellular dendrites.

3.2. Compositional analysis

Fig. 5 illustrates the distribution of the Ni, Cr and Fe elements across the FZ of the Alloy 690–SUS 304L SS weldment. The Ni and Cr contents increased with increasing BOF value because a higher BOF enhances the melting of the Alloy 690 BM. By contrast, the Fe content of the FZ was decreased with an increasing BOF value. As a consequence, the dilution of the Alloy 690 BM in the FZ by the SUS 304L SS BM was decreased as the BOF increases, and therefore the FZ has an increasingly homogeneous composition. The difference in the Ni and Cr contents of different regions of the FZ has a direct effect on the stress corrosion cracking resistance and intergranular stress corrosion cracking resistance of the weldment [21,22].

Fig. 6 shows the average Ni, Cr and Fe contents in the FZ of weldments formed using BOFs of 0, 0.15 and 0.30 mm, respectively. As shown, when the electron beam was located in the center of the weldment, i.e. BOF = 0, the average Ni, Cr and Fe contents in the FZ were 21.0 wt.%, 18.9 wt.% and 59.8 wt.%, respectively. That is to say, the composition of the FZ was closer to that of the SUS 304L SS BM than that of the Alloy 690 BM. This result was to be expected since, as discussed earlier, the thermal conductivity and specific heat of SUS 304L SS are lower than those of Alloy 690, and hence the SUS 304L SS BM melts more significantly than the Alloy 690 BM. When the BOF was set to 0.15 mm, the average Ni, Cr and Fe contents in the FZ were found to be 40.7wt.%, 25.2wt.% and 33.7wt.%, respectively. The shift of the electron beam enhanced

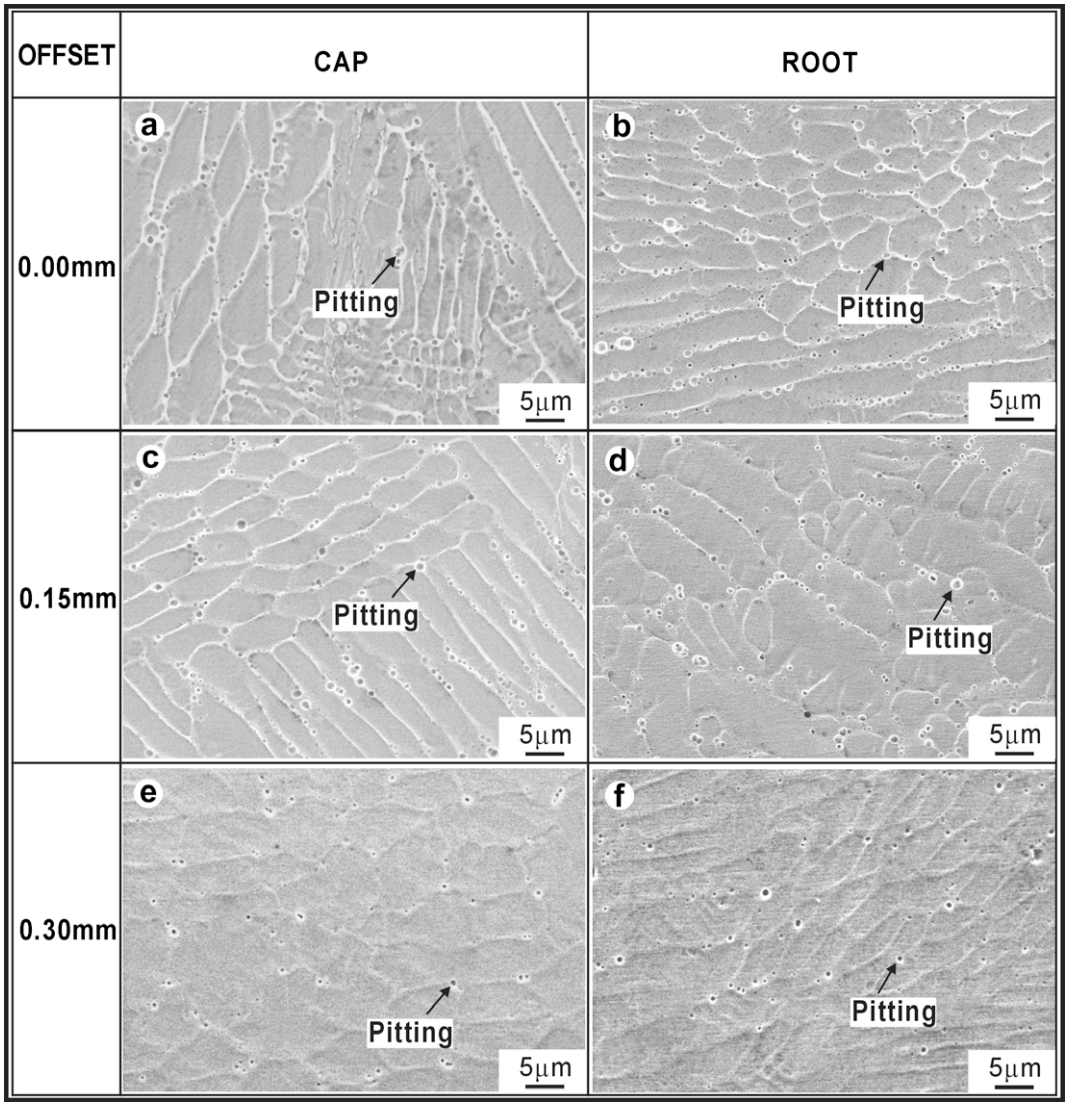

Fig. 9. Corrosion characteristics of cap and root regions in FZ of weldments formed using BOFs of 0, 0.15 and 0.30 mm.

the melting of the Alloy 690 BM, while simultaneously reducing that of the SUS 304L SS BM. Finally, when the BOF was specified as 0.30 mm, the Ni, Cr and Fe contents of the FZ were found to be 51.9wt.%, 27.9wt.% and 19.3wt.%, respectively; i.e., the composition of the FZ was close to that of Alloy 690 BM.

3.3. Mechanical property tests

Fig. 7 presents the stress–strain curves and corresponding mechanical properties of tensile testing dissimilar Alloy 690–SUS 304L SS weldments fabricated using BOFs of 0, 0.15, 0.30 and 0.50 mm, respectively. It was apparent that all of the specimens ruptured in the FZ, and thus it can be concluded that the tensile strength of the FZ was lower than that of either of the two BMs. Furthermore, Fig. 7 reveals that both the tensile strength and the total tensile elongation were decreased as the BOF was increased. When the BOF had a value of 0 mm, the electron beam was aligned with the gap, and the resulting weldment had a maximum tensile strength of 582.1 MPa because the gap helped the electron beam to penetrate the weldment [20]. When the BOF was increased to 0.30 mm, the tensile strength was reduced slightly to 541.2 MPa. However, when the BOF was further increased to 0.50 mm, the tensile strength fell significantly to 152.5 MPa, approximately 1/4 that of the specimen welded with a BOF value of 0 mm. This dramatic reduction in the tensile strength was the result of losing the function of the gap in aiding the electron beam to penetrate the weldment. Poor penetration of the weldment by the electron beam was caused by higher BOF values (see Fig. 3(d)), which in turn prevented proper fusing of the two BMs during the welding process.

Fig. 8 presents SEM images of the fracture surfaces of specimens fabricated using BOFs of 0, 0.15 and 0.30 mm, respectively. From the rupture results, it was found that all of the fracture surfaces were characterized by a dimple-like structure, which is indicative of a ductile failure mode. The density and dimensions of the dimples in the various specimens were observed to be insensitive to the value of the BOF. This observation is consistent with the finding

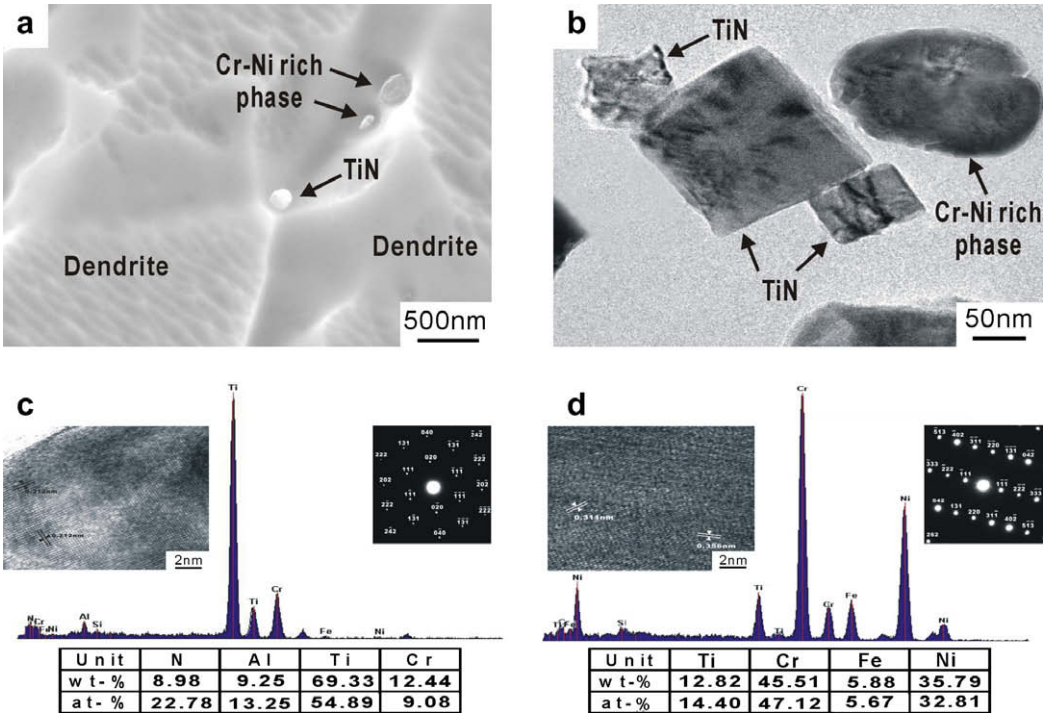

Unit	N	Al	Ti	Cr
wt-%	8.98	9.25	69.33	12.44
at-%	22.78	13.25	54.89	9.08

Unit	Ti	Cr	Fe	Ni
wt-%	12.82	45.51	5.88	35.79
at-%	14.40	47.12	5.67	32.81

Fig. 10. Micrographs and compositional analysis of interdendritic phase in weldment formed using BOF of 0.30 mm (a) SEM micrograph of interdendritic region (b) TEM micrograph of interdendritic region (carbon extraction replica), (c) representative TEM EDS spectrum of TiN (inset shows electron diffraction pattern of TiN and lattice image of TiN precipitate showing (2 0 0) d-spacing of 0.212 nm), and (d) representative TEM EDS spectrum of Cr–Ni rich phase (inset shows electron diffraction pattern of Cr–Ni rich phase and lattice image of Cr–Ni rich phase showing (2 2 0) and (3 1 1) d-spacings of 0.356 nm and 0.311 nm, respectively).

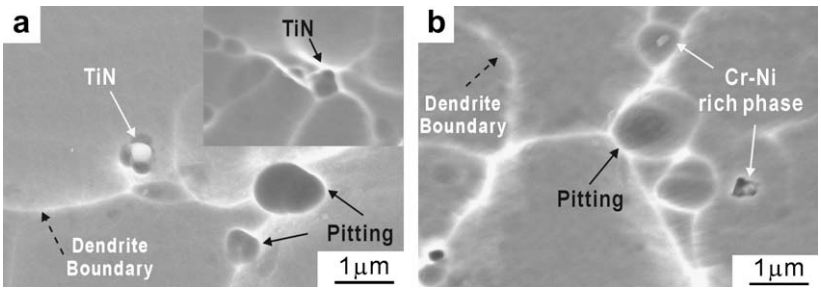

Fig. 11. SEM micrographs of precipitates in FZ of weldment formed using BOF of 0.30 mm following modified Huey test: (a) TiN precipitates (inset shows TiN pit), and (b) Cr–Ni rich phase.

above that the tensile strength of the weldment is essentially independent of the offset value when BOF $\leqslant$ 0.30 mm.

3.4. Corrosion resistance

The corrosion resistance of the various weldments was evaluated by performing modified Huey tests and potentiodynamic polarization tests, as described in the paragraphs below.

3.4.1. Modified Huey test

Fig. 9 presents SEM images of the cap and root regions of the FZ of weldments after the modified Huey test. It is clear that the corrosion was limited predominantly to the interdendritic regions of the FZ. In the EBW process, the interdendritic regions are the last solidified areas of the FZ, and therefore they always contain precipitates. The disparity in the electrochemical potentials of the precipitates and the matrix, prompts a galvanic corrosion effect in the interdendritic region. As discussed previously, the extent to which the Alloy 690 BM melts increases as the BOF is increased, and thus the Cr content of the FZ also increases. Fig. 9 also indicates that the increased Cr content improves the interdendritic corrosion resistance of the FZ; i.e., both the size and the number of the corrosive pit features were reduced as the BOF was increased.

Fig. 10 presents micrographs and a compositional analysis of the interdendritic phases formed in the FZ of a weldment fabricated using a BOF of 0.30 mm. As shown in the figure, two basic precipitates are formed, namely a rectangular phase and an oval phase. The EDS analysis results presented in Fig. 10(c) show that the content of the rectangular phase was dominated by Ti, i.e. 69.33 wt.%. Also found were chromium (12.44 wt.%), nitrogen (8.98 wt.%) and aluminum (9.25 wt.%). The precipitates of the rectangular phase are judged to be TiN from the compositions, lattice image, and electron beam diffraction patterns. TiN has a lattice parameter of 0.424 nm. Calculations based on the lattice image of Fig. 10(c) reveal that the (200) d-spacing has a value of 0.212 nm. By contrast, Fig. 10(d) shows that the oval precipitates are composed primarily of Cr (45.51 wt.%) and Ni (35.79 wt.%). Moreover, the d-spacings of the Cr–Ni rich phase are 0.356 nm by (200) d-spacing and 0.311 nm by (311) d-spacing, respectively, as shown in Fig. 10(d). However, as shown in Fig. 10(b), the Cr–Ni rich phases in the interdendritic region are quite small (i.e. in the nanometer scale). As a result, a chromium depletion zone is not formed in the FZ, and therefore the susceptibility of the weldment to interdendritic corrosion is reduced.

Fig. 11 presents SEM micrographs of the TiN and Cr–Ni rich precipitates in the FZ of a weldment fabricated using a BOF of 0.30 mm following the modified Huey test. It was observed that the corrosion occurred primarily in the matrix regions surrounding the TiN precipitates and Cr–Ni rich phases as indicated by the white arrows in Fig. 11(a and b). Pitting occurred at the dendrite boundaries in the FZ. This pitting was caused by the TiN and Cr–Ni rich phases precipitates located in the dendrite boundary regions of the FZ literally falling out of the matrix as a result of corrosion. As discussed above, the pitting corrosion observed in the FZ was caused by a disparity in the electrochemical potentials of the TiN precipitates/Cr–Ni rich phases and the matrix, which resulted in a galvanic corrosion effect at the boundaries between them [23–24]. Once the periphery of a precipitate has been completely corroded, it drops out of the matrix, resulting in the formation of a surface pit [25]. Fig. 12(a) presents a TEM image of a grain boundary in the FZ of a weldment fabricated using a BOF of 0.30 mm. It can be seen clearly from Fig. 12(a) that there are no chromium carbides to be found at the grain boundary in the FZ. Meanwhile, Fig. 12(b) illustrates the compositional variations in the Ni, Cr and Fe contents across the grain boundary. The line scan results demonstrate that the Cr content at the grain boundary remained between 28.83 wt.% and 31.30 wt.%; i.e., no significant chromium depletion occurred at the grain boundary. As a result, the effects of intergranular corrosion at the grain boundary were effectively suppressed, as confirmed in Fig. 9(e and f).

3.4.2. Electrochemical polarization behavior

Fig. 13 illustrates the potentiodynamic polarization curves obtained in weldments fabricated using BOFs of 0, 0.15 and 0.30 mm, respectively. The tests were performed in a solution of

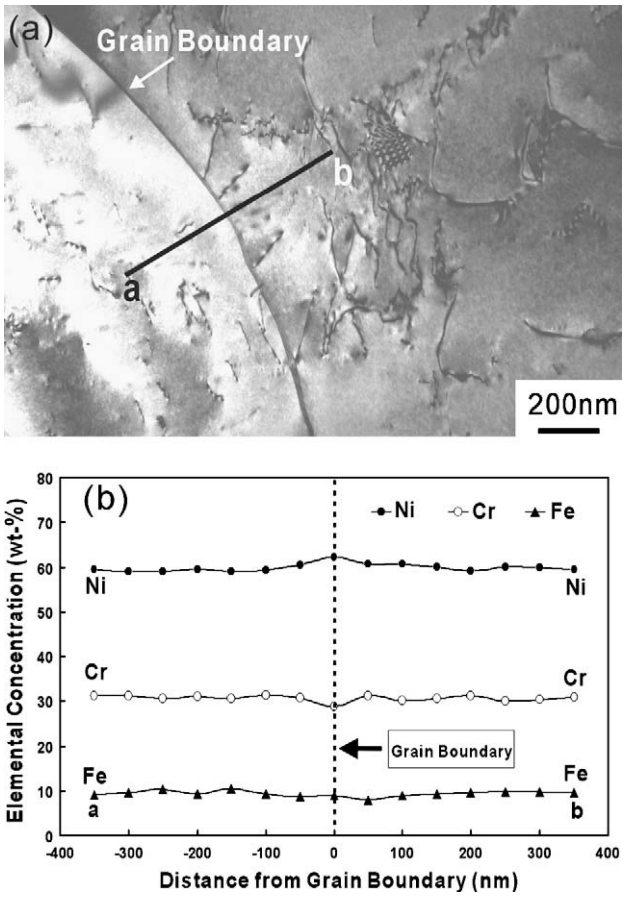

Fig. 12. Line scans across grain boundary in FZ of weldment formed using BOF of 0.30 mm (a) TEM image of a grain boundary region in FZ and (b) TEM line scan showing compositional variation across grain boundary in FZ.

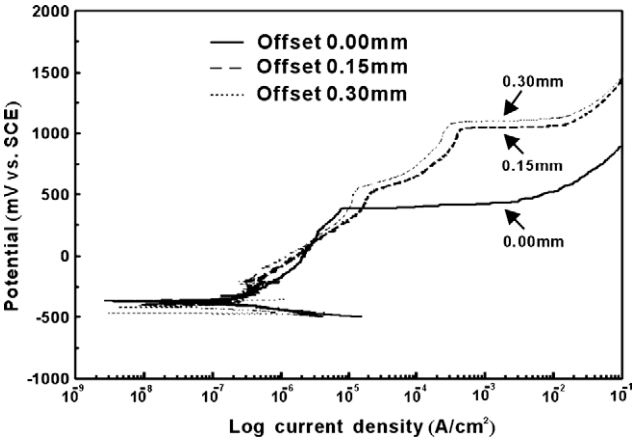

Fig. 13. Potentiodynamic polarization curves of FZ formed with BOFs of 0, 0.15 and 0.30 mm, respectively, tested in solution of 0.01 M $Na_2S_2O_3$ + 1wt.% NaCl.

0.01 M $Na_2S_2O_3$ + 1 wt.% NaCl. The figure shows clear evidence of a passivation phenomenon, with the broadening of the passivation region as the BOF increases. When the BOF was increased from 0 to 0.30 mm, the pit nucleation potential (E_{np}) values increased from 385 to 1050 mV_{SCE} (note that SCE denotes the saturated calomel electrode). Although the anode polarization curves corresponding to the weldments were quite similar, the passive current density is slightly lower and the passive potential is slightly higher with higher BOF. In other words, the Cr content of the FZ increases with an increasing BOF, and thus the pitting corrosion resistance of the FZ is enhanced.

Basically, the pitting corrosion resistance of a material can be evaluated by using the pitting resistance equivalent (PRE) index. In general, this index is defined as PRE = % Cr + 3.3% Mo + 30% N, and a higher value corresponds to an improved pitting corrosion resistance [26–27]. From this definition of PRE, it is exhibited that the alloy elements having the greatest influence on the pitting corrosion resistance of a material are chromium, molybdenum and nitrogen. For materials employed in our study, no nitrogen was found and little molybdenum (0.03wt.%) was detected in the FZ, the value of the PRE is determined chiefly by the chromium content. The PRE values of the current dissimilar weldments were found to be 19.1, 25.3 and 28.0, which indicates that the PRE value increases with an increasing BOF as a result of the higher Cr content in the FZ. These findings are consistent with results obtained in the potentiodynamic polarization tests.

4. Conclusions

(1) All of the current specimens fractured in the FZ and revealed a ductile failure mode. As the BOF increases from 0 to 0.30 mm, the tensile strength is reduced slightly, but the Cr content in the FZ increases, and hence the interdendritic corrosion resistance of the weldment is enhanced.

(2) Modified Huey test revealed that the matrix around TiN precipitates and Cr–Ni rich phases of the FZ acts as preferential sites for corrosion pit initiation. However, the EBW process suppresses the precipitation of Cr carbide at the grain boundaries in the FZ, thereby reducing the effect of intergranular corrosion.

(3) The compositional analysis results have shown that the average Ni and Cr content in the FZ increases with an increasing BOF, whereas the Fe content decreases. Furthermore, the extent to which the Alloy 690 BM diluted by the molten SUS 304L SS BM is reduced, with the result that the composition of the FZ becomes increasingly homogeneous at higher values of the BOF.

(4) The potentiodynamic polarization tests performed using a 0.01 M $Na_2S_2O_3$ + 1wt.% NaCl solution have shown that E_{np} increases from 385 mV_{SCE} in the FZ fabricated using a BOF of 0.00 mm to 1050 mV_{SCE} in the FZ formed using a BOF of 0.30 mm. The higher value of E_{np} implies that the FZ has an improved pitting corrosion resistance as a result of a higher Cr content.

Acknowledgements

The current authors gratefully acknowledge the financial support provided to this study by the National Science Council of Taiwan, under Grant No. NSC 9l-2626-E-232-002.

References

[1] T. Ishihiara, Weld. J. 68 (1989) 209–216.
[2] S. Kou, Welding Metallurgy, Wiley, New York, 1987.
[3] B.E. Payne, Met. Constr. 1 (1969) 79–86.
[4] J.D. Kim, J.H. Moon, Corros. Sci. 46 (2004) 807–815.
[5] G. Sui, J.M. Titchmarsh, G.B. Heys, J. Congleton, Corros. Sci. 39 (1997) 565–573.
[6] K. Stiller, J.O. Nilsson, K. Norring, Metall. Mater. Trans. A 27A (1996) 327–341.
[7] T.Y. Kuo, H.T. Lee, Mater. Sci. Eng. A 338 (2002) 202–212.
[8] H.T. Lee, S.L. Jeng, Sci. Technol. Weld. Joining 6 (2001) 225–234.
[9] H.T. Lee, T.Y. Kuo, Sci. Technol. Weld. Joining 4 (1999) 94–103.
[10] R.M. Horn, G.M. Gordon, F.P. Ford, R.L. Cowan, Nucl. Eng. Des. 9 (1997) 313–325.
[11] S.L. Jeng, H.T. Lee, W.P. Rehbach, T.Y. Kuo, J.P. Mayer, Mater. Sci. Eng. A 397 (2005) 229–238.
[12] H.T. Lee, S.L. Jeng, C.H. Yen, T.Y. Kuo, J. Nucl. Mater. 335 (2004) 59–69.
[13] H.T. Lee, S.L. Jeng, T.Y. Kuo, Metall. Mater. Trans. A 34 (2003) 1097–2005.
[14] T.Y. Kuo, H.T. Lee, C.C. Tu, Sci. Technol. Weld. Joining 8 (2003) 39–48.
[15] H.J. Stone, S.M. Roberts, R.C. Reed, Metall. Mater. Trans. A 31A (2000) 2261–2273.
[16] Z. Sun, R. Karppi, J. Mater. Process. Technol. 59 (1996) 257–264.
[17] Y.S. Lim, J.S. Kim, H.S. Kwon, Mater. Sci. Eng. A 279 (2000) 192–200.
[18] Y.S. Kim, J.H. Suh, I.H. Kuk, J.S. Kim, Metall. Trans. A 28A (1997) 1223–1231.
[19] A. Czyrska-Filemonowicz, K. Spiradek, Eur. Microsc. Anal. 3 (1995) 13–14.
[20] A. Salminen, A. Fellman, V. Kujanpaa, Proc. SPIE 5336 (2004) 84–94.
[21] A.J. Sedriks, S. Floreen, A.R. Mcllree, Corrosion 32 (1976) 157–158.
[22] H. Nagano, K. Yamanaka, K. Kobayashi, M. Inoue, Sumitomo Metals 40 (1988) 17–28.
[23] W.T. Tsai, C.L. Yu, J.I. Lee, Scripta Mater. 53 (2005) 505–509.
[24] L. Reclaru, R. Lerf, P.Y. Eschler, J.M. Meyer, Biomaterials 22 (2001) 269–274.
[25] I.H. Lo, W.T. Tsai, Mater. Sci. Eng. A 355 (2003) 137–143.
[26] M.O. Speidel, in: Proceedings of International Conference on Stainless Steels, Chiba, Japan, 10–13 June 1991, Springer, Tokyo, 1991, pp. 25–26.
[27] C.M. Tseng, W.T. Tsai, Mater. Chem. Phys. 84 (2004) 162–170.